Effect of Mach number and volume fraction in air-shock interacting with a bed of randomly distributed spherical particles

Y. Mehta,[1] K. Salari,[2] T. L. Jackson,[1] and S. Balachandar[1]
[1]*Department of Mechanical and Aerospace Engineering, University of Florida, Gainesville, Florida 32611, USA*
[2]*Lawrence Livermore National Laboratory, Livermore, California 94550, USA*

(Received 14 August 2018; published 15 January 2019)

Shock-particle interaction is a fundamental problem in many engineering applications, with the dynamics being heavily influenced by the incident-shock Mach number and the particle volume fraction. In this paper we present fully resolved inviscid simulations of an incident-shock wave traveling through a bed of randomly distributed spherical particles. We vary the strength of the incident shock along with the particle volume fraction in order to study the complex wave interaction during shock-particle interaction. In this study we are interested in the early-time behavior during which the particles do not move and hence in our simulations all the particles are fixed in space. We compute the streamwise average of flow field quantities to generate the x-t contour plots to study the unsteady oscillations inside the particle bed. We observe that the transmitted shock slows down under certain conditions and it is partly due to tortuosity and partly due to weakening caused by energy dissipation. We also present the force histories of the streamwise drag and lift forces for all the particles. The random distribution of particles leads to high variability in the drag force experienced by the particles. We compute the mean peak drag force as a function of the streamwise location to study the mean behavior of the transmitted shock. Based on our findings, we propose simple modifications to improve the current point-particle models used in Euler-Lagrange simulations of shock interacting with a bed of particles.

DOI: 10.1103/PhysRevFluids.4.014303

I. INTRODUCTION

It is important to understand the dynamics of a shock interacting with a bed of particles due to its extensive industrial applications [1–5] and occurrence in nature [6,7]. Currently, there is a lack of understanding and data in terms of the physical mechanisms at play during shock interacting with a bed of particles and the forces experienced by the particles. The primary goal of this study is to fill this knowledge gap by performing fully resolved inviscid simulations of an incident shock traveling through a bed of monodispersed randomly distributed spherical particles. We note that in a fully resolved simulation the standard governing equations (Navier-Stokes or Euler) are solved by resolving the flow to the finest relevant scale. In the Euler simulations that are discussed here, the smallest relevant spatial scale is the particle diameter apart from the shock thickness. We vary the strength of the incident shock and the particle volume fraction to study the effect of these two parameters on the flow field and the forces experienced by the particles.

Previously, shock interaction with a single particle has been studied in depth by various researchers [8–12] by carrying out experiments and performing numerical simulations. Recently, a number of fully resolved numerical simulations of shock interacting with multiple cylinders [13–15] and multiple spheres [16–18] have been reported. For example, Sridharan *et al.* [16] investigated the effect of interparticle spacing and incident-shock Mach number on the drag force experienced by spherical particles arranged one after the other in a simple one-dimensional horizontal array. Mehta

et al. [17] carried out simulations of shock interaction with a one-dimensional transverse array of particles and reported that in some cases the secondary wave interactions due to fluid-mediated particle-particle interaction can lead to forces higher than those induced by the incident shock. Mehta *et al.* [18] reported results from numerical simulations of incident shock interacting with a face-centered-cubic array of particles. They varied the incident-shock Mach number and particle volume fraction to study the effect of these parameters on the streamwise drag force experienced by the particles. The complex physical mechanisms occurring during shock-particle interaction were identified and their effect on the overall flow and the drag forces experienced by the particles was studied.

More recently, Mehta *et al.* [19] performed fully resolved three-dimensional inviscid simulations of an incident shock propagating through a random bed of monodispersed spherical particles, similar to the one considered in this study. They varied the particle volume fraction but held the incident-shock Mach number M_s constant at 3. They reported that the random distribution of the particles significantly altered the force history of each particle compared to that of an isolated particle, and the fluid mediated particle-particle interaction resulted in high variability in the peak streamwise drag force experienced by each particle. It was also found that the incident shock weakened as it traveled through the particle bed. The weakening of the incident shock was attributed to dissipation of energy due to formation of shocklets and bow shocks inside the particle bed.

The goal of this work is to extend the simulations of Mehta *et al.* [19] to cases where the incident-shock Mach number is smaller than $M_s = 3$. We note that the critical Mach number for an isolated particle is 0.6. If the relative Mach number of the postincident-shock flow is equal to or greater than the critical Mach number then the flow will accelerate locally over the particle to reach sonic or supersonic velocity. For a given incident shock, the postincident-shock flow can have three regimes based on its Mach number M_{ps}. These distinct flow regimes are subsonic and subcritical ($M_{ps} < 0.6$), subsonic and supercritical ($0.6 \leqslant M_{ps} < 1$), and supersonic and supercritical ($M_{ps} \geqslant 1$). The inviscid flow behavior for these different flow regimes is distinctly different and results in unique flow features around the particles. For $M_{ps} \geqslant 1$ a bow shock will form upstream of the particle and for $0.6 \leqslant M_{ps} < 1$ a shocklet will form along the particle surface. Both of these flow regimes are supercritical and the steady-state streamwise drag force on a particle will be nonzero. Both the bow shock and the shocklet also dissipate energy from the flow resulting in weakening of the incident or transmitted shock as it travels through the particle bed [18,19]. For $M_{ps} < 0.6$ the reflected waves are weak compression waves and the postincident-shock inviscid drag force on a particle will be zero. As mentioned previously, the critical Mach number stated here is for an isolated spherical particle and we expect it to be different for a bed of particles. In fact, the critical Mach number for a bed of particles will depend on the particle volume fraction along with the incident-shock Mach number.

In view of the above observations, we consider three incident-shock Mach numbers $M_s = 1.22$, 1.66, and 3. The corresponding postincident-shock Mach numbers are $M_{ps} = 0.31$, 0.73, and 1.36, respectively, which covers all three flow regimes discussed above. The particle volume fraction ϕ_1 is also varied from 2.5% to 10% to 20%. Varying the incident-shock Mach number and particle volume fraction results in nine unique combinations for the numerical simulations. The numerical simulations performed in this study can be thought of as virtual experiments, where we can study the effect of the particle volume fraction and the incident-shock Mach number on the particles and investigate the effect of the particles on the flow under certain specific conditions during shock propagation. For all the simulations considered here, we observe large particle-to-particle variations in the drag force. The unsteady flow inside the particle bed due to the secondary wave interactions and locally oblique shocks results in transverse forces on the particles. The magnitude of the transverse forces can be up to 40% of the streamwise drag force and hence will have a significant impact on the particle motion at later times and also on the overall flow dynamics. Fluid-mediated particle-particle interaction after passage of the incident shock can sometimes lead to forces much higher than the drag force induced by the incident shock on the particles. These effects due to presence of multiple particles are not captured by the current point-particle force models (see, for example, [20–23]).

We also observe that for some of the simulations presented here the transmitted shock slows down as it travels through the particle bed. Depending on the incident-shock Mach number and the particle volume fraction, the transmitted shock slowing down is due to either tortuosity or a combination of tortuosity and transmitted shock weakening. The presence of particles results in a tortuous path for the transmitted shock and causes it to slow down. For simulations with supercritical postincident-shock flow the transmitted shock weakening can be attributed to the formation of shocklets and bow shocks, which dissipate energy from the flow. For $M_s = 1.22$ and $\phi_1 = 10\%$ and 20%, the postincident shock can reach sonic or supersonic velocities inside the particle bed at later times due to nozzling of the flow. We compute the vorticity magnitude inside the computational domain to measure the baroclinic generation of vorticity. We also compute the streamwise average of flow quantities like pressure, density, and velocity to characterize the strength of the reflected waves and the transmitted shock, along with the fluctuations inside the particle bed. Finally, we present three-dimensional isosurface contour plots of velocity magnitude to identify the various flow features resulting due to shock interaction with the particle bed.

This paper is organized as follows. In Sec. II we discuss the governing equations, the numerical method, and the simulation setup employed in this study. The results of the numerical simulations are presented in Sec. III, where we present the contour plots of flow properties and x-t plots for all the simulations and discuss the slowing down of the transmitted shock followed by the force histories of all the particles. In Sec. IV we present a summary and the conclusions.

II. NUMERICS

In this paper we investigate an air-shock interacting with a bed of randomly distributed monodispersed spherical particles, similar to that considered by Mehta *et al.* [19]. We limit our discussion to early times during which viscous mechanisms are weak and thermal effects are negligible. In prior work we discussed the importance of the timescales associated with the problem of shock-particle interaction [18] and validity of neglecting viscous effects and particle motion during early times. Hence, we solve the standard three-dimensional Euler equations and the system of equations is closed by assuming an ideal gas equation of state for air. These equations are solved using a finite-volume method with body-conforming unstructured tetrahedral meshes (see [19] for details). An exhaustive grid resolution study for this setup was previously performed by Mehta *et al.* [18,19] and grids used for this study follow the guidelines provided by them to minimize the numerical error along with minimizing the computational cost.

Shock interaction with a particle leads to unsteady forces on the particle. In this investigation we present these unsteady forces in terms of the nondimensional drag coefficient given by

$$\vec{C}_D = \frac{\vec{F}}{\frac{1}{2}\rho_{ps} u_{ps}^2 A}, \tag{1}$$

where $\vec{F}$ is the force, ρ_{ps} the postincident-shock density, u_{ps} the corresponding postincident-shock velocity, and A the cross-sectional area of the particle. For a sphere, $A = \pi d_p^2/4$, where d_p is the particle diameter.

In this study we vary the particle volume fraction ϕ_1 from 2.5% to 20% and the incident-shock Mach number M_s is varied from 1.22 to 3, resulting in nine combinations of ϕ_1 and M_s for the simulations. The three-dimensional simulation setup is shown in Fig. 1. Along the streamwise direction the computational domain is separated into an upstream shocked region (red) without particles, x_{upstream}, and a downstream quiescent ambient region (blue) containing a random distribution of particles, x_{part}. The leftmost edge of the particle curtain is located at $x/d_p = 0$. The computational domain details for all the particle volume fractions considered in this study are given in Table I. The transverse length of the computational domain is given as $(y, z)/d_p$ in Table I.

To characterize the random distribution of particles, we compute the local volume fraction associated with each particle. VORO++ [24], a three-dimensional Voronoi library, is used to compute

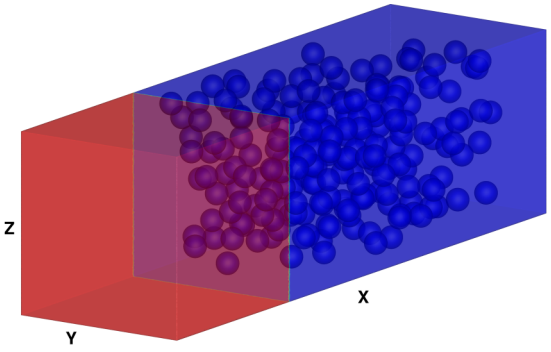

FIG. 1. Simulation setup at time zero.

the local volume fraction $\phi_{i,1}$ associated with each particle. Based on the local volume, we compute the fluctuation in the local volume fraction ϕ_{flu_i} for each particle and it is given by

$$\phi_{flu_i} = \frac{\phi_{i,1} - \phi_1}{\phi_1}. \tag{2}$$

Here ϕ_{flu_i} is the relative difference between the local volume fraction of ith particle and the global particle volume fraction ϕ_1. The histograms of the distributions for ϕ_{flu_i} for $\phi_1 = 2.5\%$, 10%, and 20% are plotted in Figs. 2(a), 2(b), and 2(c), respectively. A normal distribution fit is obtained for the data and plotted as the red curve in Fig. 2. The local volume fraction fluctuation is due to the random distribution of the particles and follows a Gaussian-like distribution.

The unshocked state is quiescent ambient air with $P_1 = 101.325$ (kPa) and $\rho_1 = 1.2048$ (kg/m^3). The postincident-shock conditions for an incident air shock are determined by the Rankine-Hugoniot relations for an ideal gas with $\gamma = 1.4$ and $R = 287.04$ (J/kg K). Note that the postincident-shock pressure p_{ps} for all the shock Mach numbers considered in this study remains well below the yield strength for most materials (0.2 GPa) and so we do not expect the particles to deform.

The upstream or the left boundary of the domain is treated as a constant inflow boundary with inflow set at postincident-shock properties. All the other boundaries, including the particle surfaces, are treated as slip walls.

III. NUMERICAL SIMULATION RESULTS

In this section we present numerical simulation results of an incident shock propagating through a random bed of particles that are held fixed in space. We compute the individual force histories for all the particles as well as the peak streamwise drag force experienced by each particle. The objectives of this study are twofold: (i) to find out the effect of the particles on the incident shock and its behavior as it travels through the particle bed and (ii) to find the impact of the incident shock on a random bed of particles in terms of the forces experienced by them. To this end we compute the cross-streamwise planar average of flow field properties like pressure and velocity to compute the strength of the transmitted shock and generate x-t contour plots to identify the different physical

TABLE I. Computational domain details for the particle volume fractions considered in this study.

ϕ_1	d_p (μm)	N_p	x_{part}/d_p	x_{upstream}/d_p	$(y, z)/d_p$
2.5%	50	400	33	16	16
10%	100	200	17	9	8
20%	100	400	17	9	8

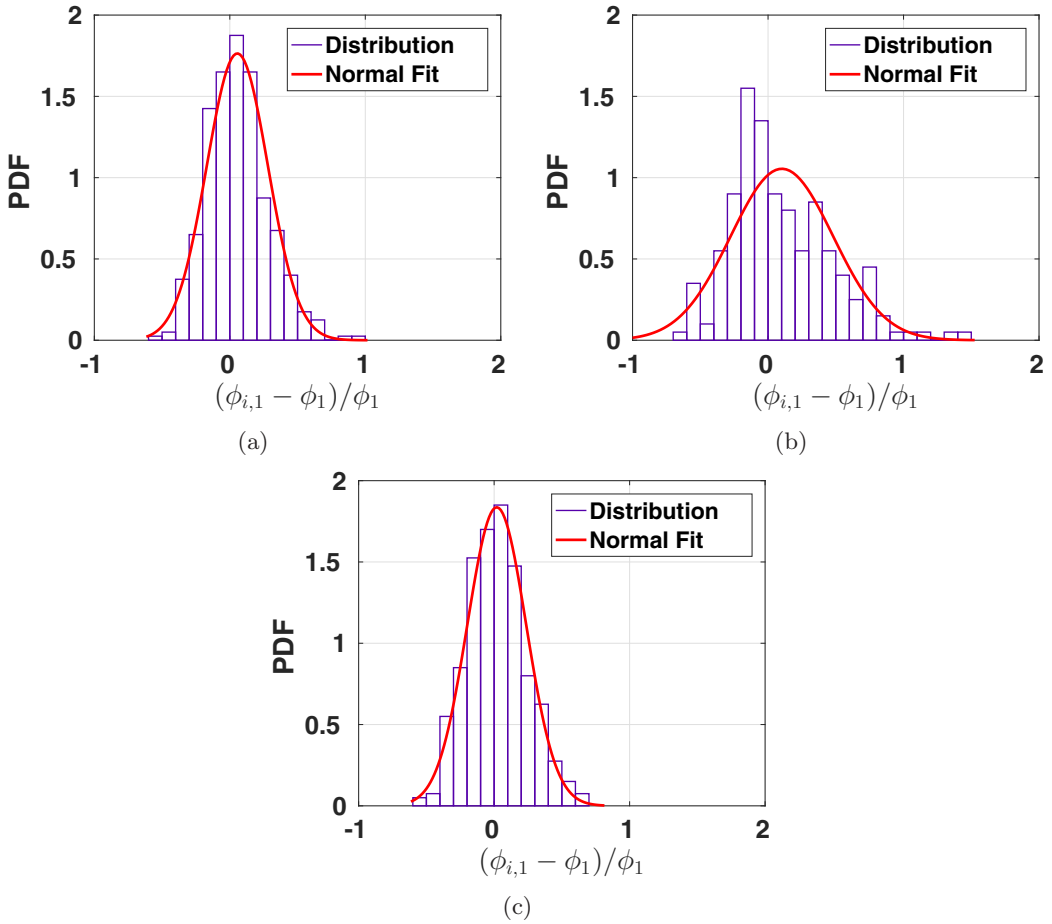

FIG. 2. Histogram plot of ϕ_{flu_i} along with the normal fit for (a) $\phi_1 = 2.5\%$, (b) $\phi_1 = 10\%$, and (c) $\phi_1 = 20\%$.

mechanisms at play during shock-particle interaction. We also present the force histories for all the particles and compute the mean peak drag force to gain insights on the drag force variability.

A. Flow-field plots

In this section we study the effect of the particles on the flow. An incident-shock impingement on a bed of particles results in complex wave dynamics; i.e., a transmitted shock propagates through the particle bed and a reflected wave travels upstream, and there are complex wave interactions inside the particle bed. Contour plots of nondimensional pressure, Mach number, and nondimensional vorticity magnitude are presented in Figs. 3–5. Note that the figures paint a picture of the flow field at one particular instant of time, but in reality the flow is transient and highly unsteady with three-dimensional flow features.

To highlight the three-dimensional nature of the problem and to observe the complex wave structure inside the particle bed, we present isosurface plots of the velocity magnitude in Fig. 3. The velocity magnitude u_{mag} has been nondimensionalized by u_{ps}. Results for $M_s = 3$ and $\phi_1 = 2.5\%$ and 20% are presented in Figs. 3(a) and 3(b), respectively. The nondimensional velocity magnitude for Fig. 3(a) is 0.6 and for Fig. 3(b) is 0.4. In both figures we observe wakes that form behind the particles. For the $\phi_1 = 2.5\%$ case we can observe that the reflected shock has not fully formed

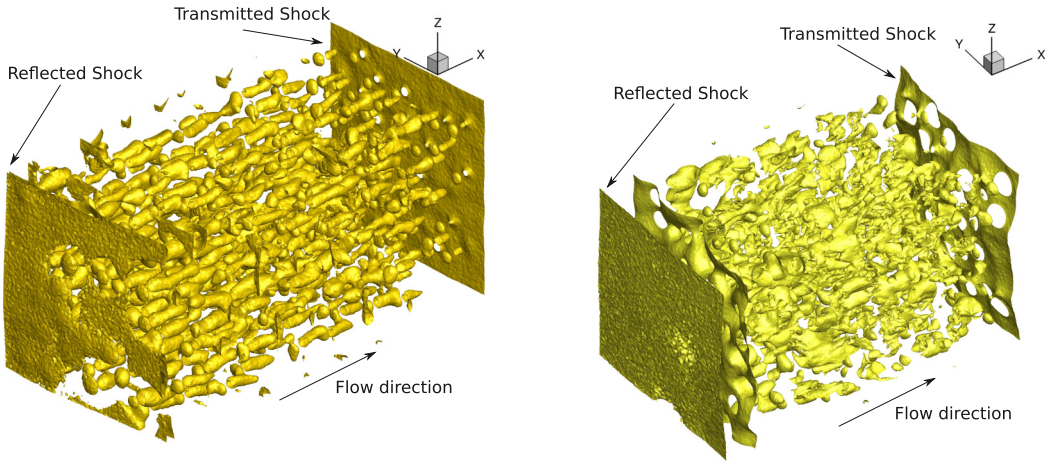

(a) (b)

FIG. 3. Isosurface plot of the nondimensional velocity magnitude for $M_s = 3$ and for (a) $\phi_1 = 2.5\%$ and (b) $\phi_1 = 20\%$.

yet, but we can observe the nearly planar transmitted shock at the far end of the particle bed. For $\phi_1 = 20\%$ we can observe the reflected shock and the transmitted shock along with the stationary wave that forms at the front edge of the particle bed.

Two-dimensional contour plots of flow properties are presented in Figs. 4 and 5. A cut section is taken through the three-dimensional computational domain. The white circles in the figures

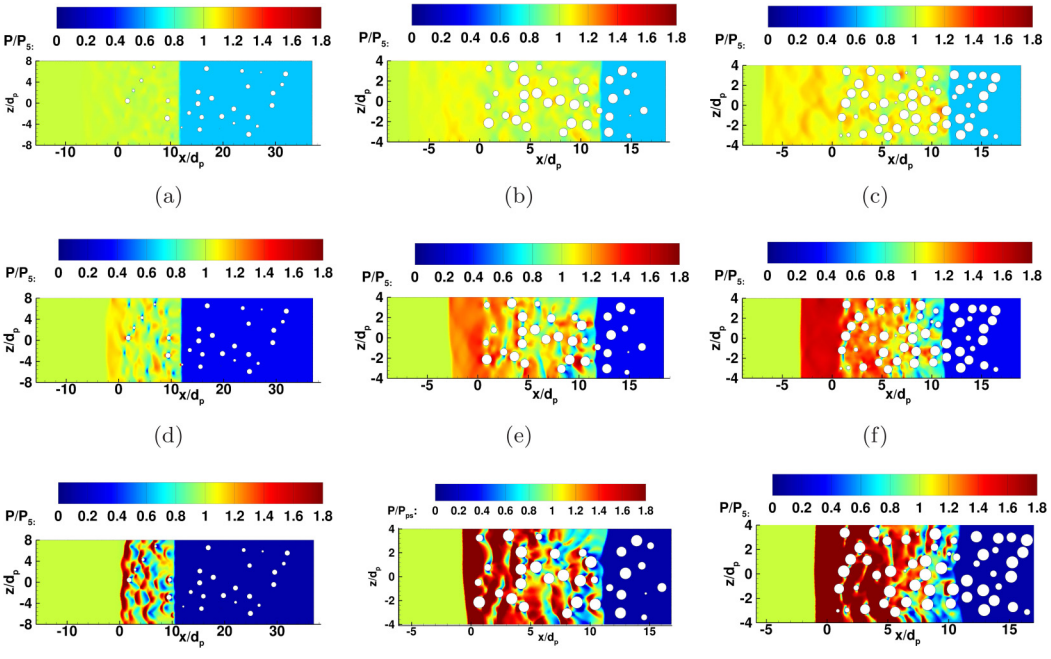

FIG. 4. Contour plot of nondimensional pressure at $t/\tau = 12$ along the x-z plane at $y = 0$ for $\phi_1 = 2.5\%$, 10%, and 20% and (a)–(c) $M_s = 1.22$, (d)–(f) $M_s = 1.66$, and (g)–(i) $M_s = 3$, respectively.

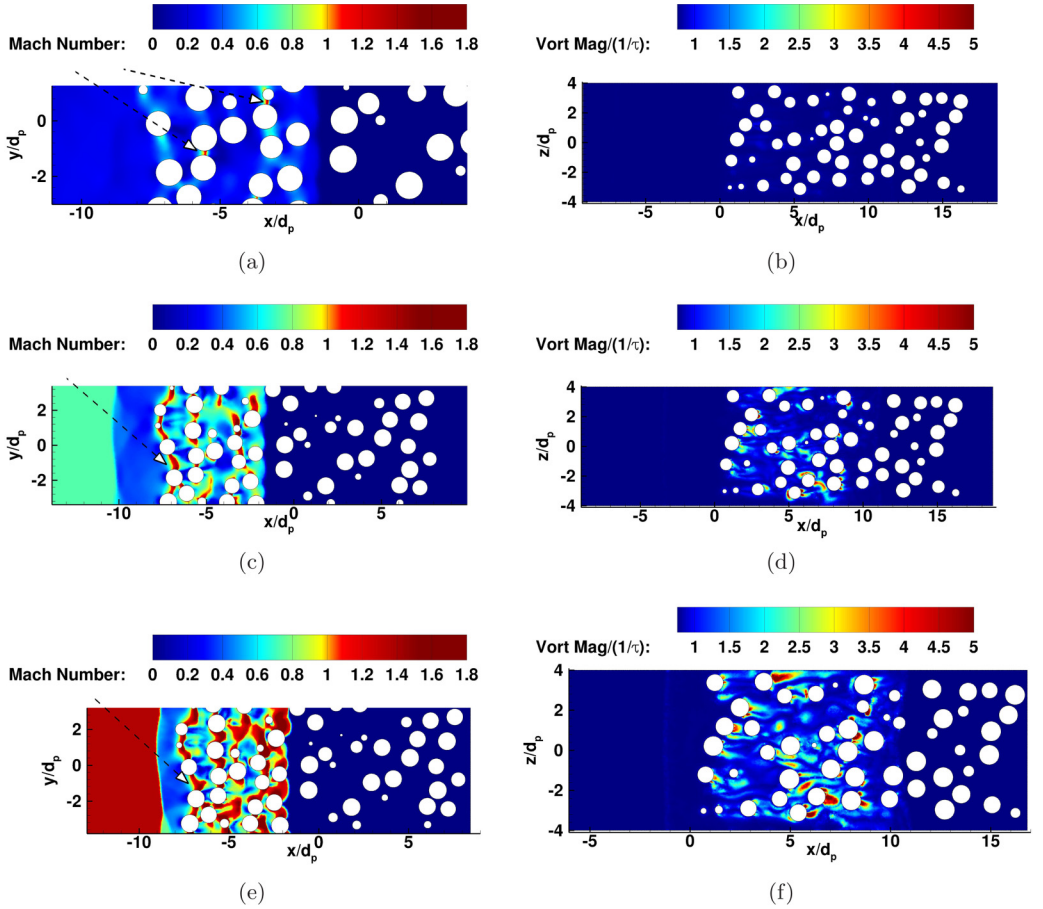

FIG. 5. Zoomed-in contour plot of the Mach number along the x-y plane at $z = 0$ and $t/\tau = 7$ for (a) $M_s = 1.22$, (c) $M_s = 1.66$, and (e) $M_s = 3$ and contour plot of the nondimensional vorticity magnitude along the x-z plane at $y = 0$ and $t/\tau = 12$ for (b) $M_s = 1.22$, (d) $M_s = 1.66$, and (f) $M_s = 1.66$, with $\phi_1 = 20\%$.

represent the particles in the computational domain. Contour plots of nondimensional pressure along the x-z plane at $y = 0$ and $t/\tau = 12$ are plotted in Fig. 4. For $M_s = 1.22$ [Figs. 4(a)–4(c)] it is clear that the reflected waves for all the particle volume fractions are quite weak. In fact, it is difficult to observe the reflected waves traveling upstream of the particle bed for the cases of $\phi_1 = 2.5\%$ and 10%. We can observe a weak reflected shock traveling upstream for the case $\phi_1 = 20\%$. This behavior indicates that the reflected compression waves for $M_s = 1.22$ and low particle volume fractions are weak and do not coalesce to form a reflected shock, but they are strong enough for the case of $\phi_1 = 20\%$ to form a reflected shock. For all three particle volume fractions there are small oscillations in the pressure field inside the particle bed. For $M_s = 1.66$ and 3 and all three particle volume fractions considered here, we can clearly observe the signature of the reflected shock and the transmitted shock. The magnitude of the wave oscillations also increases as compared to $M_s = 1.22$ case. We observe the wakes that form behind the particles and shocklets stretching out from the particles because of locally supercritical flow around the particles. The transmitted shock exhibits a corrugated structure as it deforms around the particles and a nonplanar shock will result in transverse forces on the particles. The reflected shock is formed by coalescence of individual reflected waves from the particles and requires a finite time to form. The strength of the reflected shock and the time it takes to form is affected by the particle volume fraction. This

can be observed in Figs. 4(d)–4(f) and 4(g)–4(i), where the reflected shock has barely formed for $\phi_1 = 2.5\%$, whereas it is slightly more developed for $\phi_1 = 10\%$, but it is not yet planar, while it is fully formed and planar for $\phi_1 = 20\%$.

Contour plots of Mach number for $\phi_1 = 20\%$ along the x-y plane at $z = 0$ and $t/\tau = 7$ are presented in Figs. 5(a)–5(c) for $M_s = 1.22$, 1.66, and 3, respectively. These contour plots are enhanced to focus on the flow inside the particle bed. The overall qualitative behavior of the Mach number contour plots is similar to that of the pressure plots. Even though the postincident-shock Mach number for $M_s = 1.22$ is well below the critical Mach number (0.6), we can observe that locally it accelerates to supersonic velocities (indicated by the arrows). This acceleration of the flow can be attributed to local nozzling of the flow due to the presence of particles. This will result in nonzero postincident-shock drag force on the particles and can also lead to dissipation of energy and hence weakening of the transmitted shock. For $M_s = 1.66$ and 3, the postincident-shock Mach number is supercritical and we can see shocklets extending from particle to particle (indicated by the arrow). Also, we can observe wakes forming behind the particles. As mentioned earlier, formation of shocklets and secondary wave interactions leads to nonzero drag forces on the particles at later times and weakening of the transmitted shock due to dissipation of energy. The strength of the reflected wave increases as the particle volume fraction increases for a given incident-shock Mach number, highlighting the effect of the particle volume fraction. From the contour plots it is clear that each particle has a slightly different flow field around it and will result in particle-to-particle variation in the drag force.

We plot the nondimensional vorticity magnitude in Figs. 5(d)–5(f) for $\phi_1 = 20\%$ and $M_s = 1.22$, 1.66, and 3, respectively, along the x-z plane at $y = 0$ and $t/\tau = 12$. The vorticity magnitude is nondimensionalized by the inverse of the shock timescale τ. Since we are performing inviscid simulations, vorticity generation is due to baroclinic mechanism. Previously, we performed simulations of shock interacting with structured (simple cubic and face-centered-cubic) arrays of particles and found out that vorticity production was negligible under similar conditions that are considered here. Therefore, we believe that vorticity generation in this study is a result of breakage of symmetry due to the random distribution of particles. The impact of numerical dissipation on the vorticity magnitude is negligible as previously reported by Mehta *et al.* [19]. For $M_s = 1.22$ the vorticity magnitude is negligible for all the particle volume fractions considered in this study. The vorticity magnitude for low particle volume fraction of $\phi_1 = 2.5\%$ and Mach numbers 1.66 and 3 is also negligible. For $M_s = 1.66$ and 3, the vorticity magnitude increases as the particle volume fraction increases from 10% to 20%. We can observe that most of the vorticity is concentrated in the wakes behind the particles. Particles that are downstream and in the wake of the upstream particles will experience Saffman-lift-like vorticity-induced force. Current point-particle drag models do not account for rotational forces, even though their impact on the motion of the particles and overall flow might be significant.

B. Cross-sectional average of the flow properties

It is clear from the flow field contour plots that a complex wave structure is set up inside the particle bed once the incident shock travels through it. To characterize the strength of these waves we compute the planar spatial average of density, pressure, and streamwise velocity at different streamwise locations as a function of time. The averaging process employed in this study is similar to the one previously used by Mehta *et al.* [19]. The computational domain is divided into 200 slices along the y-z plane for $\phi_1 = 10\%$ and 20% and 400 slices for $\phi_1 = 2.5\%$ and the flow properties are averaged on each slice. The cross-sectional average of a flow variable $F(x, y, z, t)$ is defined as

$$\langle F \rangle(x, t) = \frac{1}{A_g} \int_{L_y} \int_{L_z} I_g(x, y, z) F(x, y, z, t) dy\, dz, \tag{3}$$

where L_y and L_z are the sizes of the computational domain along the transverse directions. Here $I_g(x, y, z)$ is the indicator function that identifies the region occupied by the gas; $I_g = 1$ in the

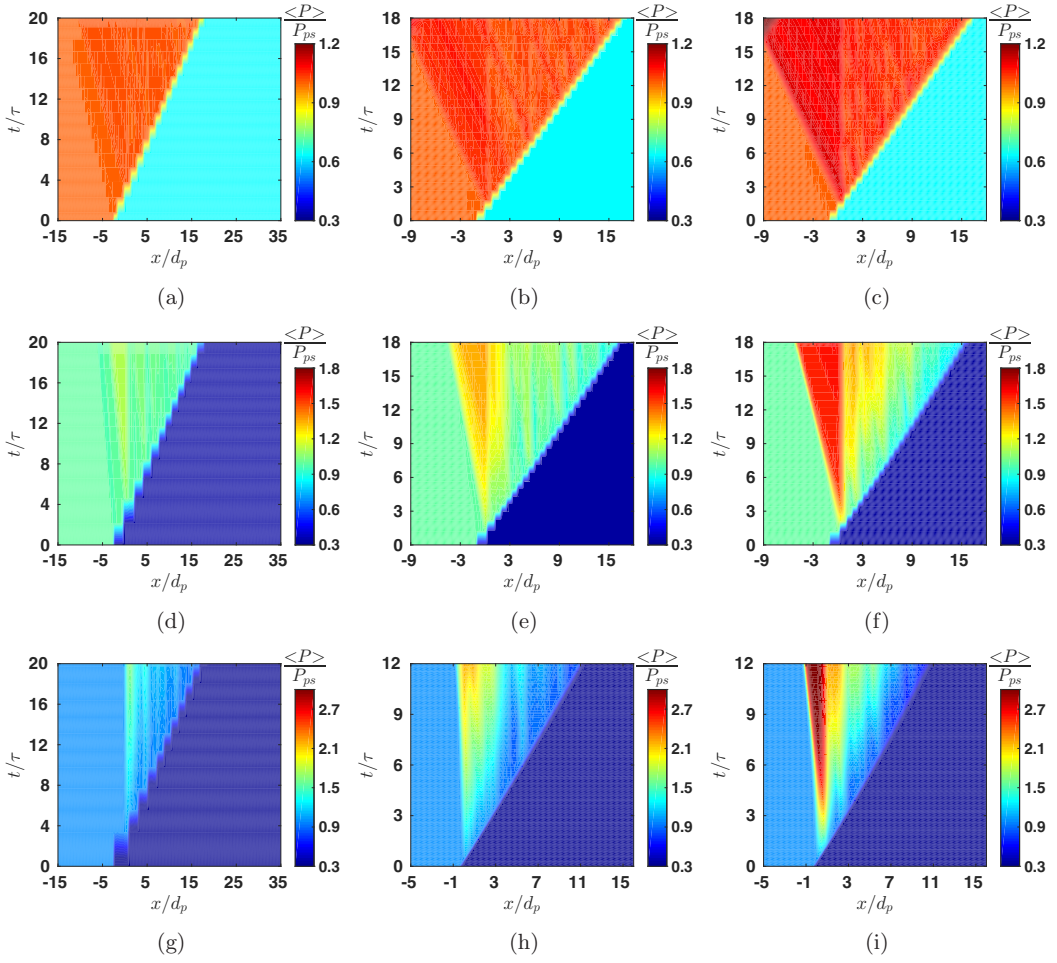

FIG. 6. The x-t contour plot of the nondimensional cross-sectional averaged pressure $\langle P\rangle/P_{ps}$ for $\phi_1 =$ 2.5%, 10%, and 20% and (a)–(c) $M_s = 1.22$, (d)–(f) $M_s = 1.66$, and (g)–(i) $M_s = 3$, respectively.

gas and $I_g = 0$ inside the particle. Thus, the integral is defined only over the cross-sectional area occupied by the gas and correspondingly $A_g = \int_{L_y}\int_{L_z} I_g(x, y, z)dy\,dz$ is the cross-sectional area occupied by the gas. The averaging process results in the data being a function of x and t.

The averaged flow properties are nondimensionalized by the corresponding postincident-shock properties. We generate x-t contour plots of the averaged data and plot them in Figs. 6 and 7. These plots provide interesting insights into the effect of the particles on the overall flow. We can observe the signature of the transmitted shock (right-moving front) and the reflected wave (left-moving front). Note that the zigzag (steplike) pattern observed for the transmitted shock in some of the x-t plots is due to the interpolation of the data (having fewer data points in time compared to x). The cross-sectional average pressure inside the particle bed for $M_s = 1.22$ and $\phi_1 = 2.5\%$ and 10% is nearly constant, indicating that the flow is nearly steady (on average) with some minor fluctuations. For $M_s = 1.66$ and 3 and all the particle volume fractions considered in this study, the reflected wave is a shock, whose strength increases as the incident-shock Mach number and particle volume fraction increase. As the particle volume fraction increases from 2.5% to 10% to 20%, we can observe that oscillations appear inside the particle bed and their strength increases as the incident-shock Mach number increases. For a fixed particle volume fraction the speed of the

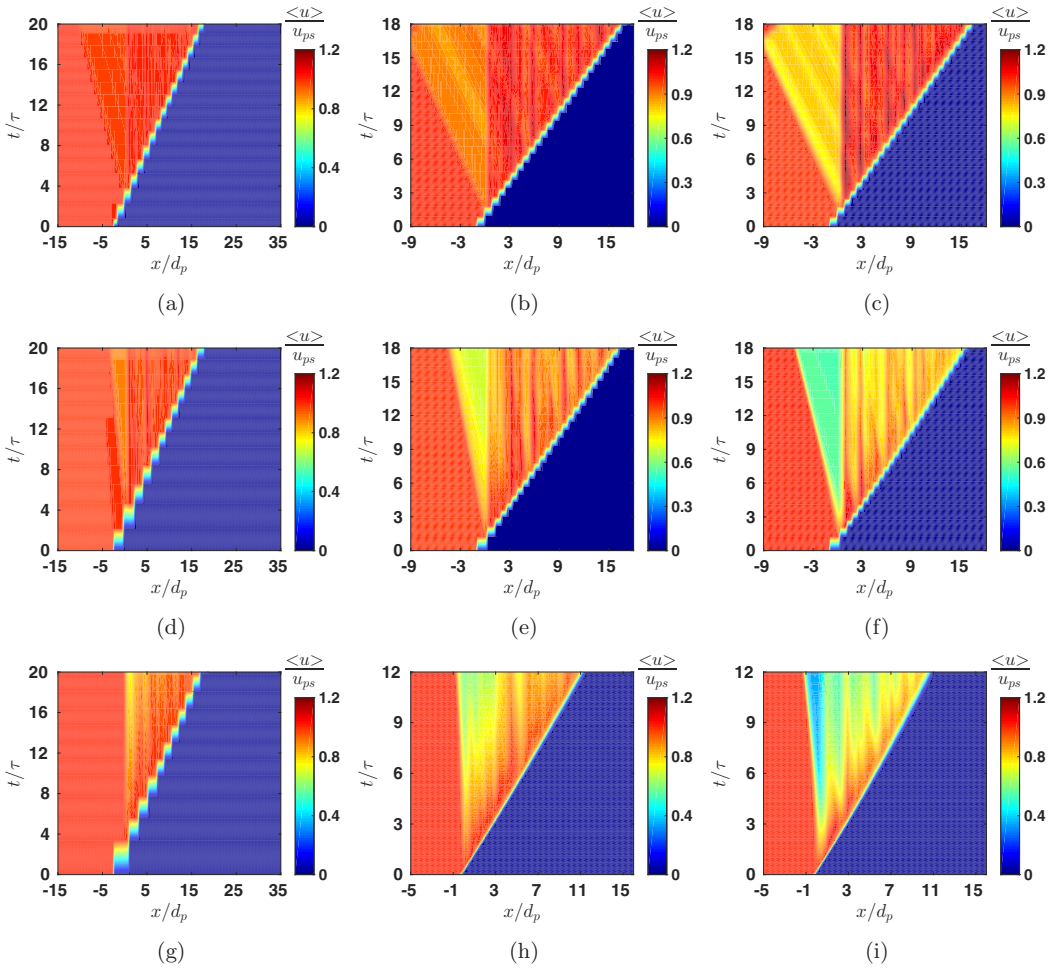

FIG. 7. The x-t contour plot of the nondimensional cross-sectional averaged streamwise velocity $\langle u \rangle / u_{ps}$ for $\phi_1 = 2.5\%$, 10%, and 20% and (a)–(c) $M_s = 1.22$, (d)–(f) $M_s = 1.66$, and (g)–(i) $M_s = 3$, respectively.

reflected wave decreases as the incident-shock Mach number increases. This is because the speed of the postincident-shock flow, which is in the opposite direction of the reflected shock, also increases.

It is interesting to observe from the x-t plots that the flow properties change abruptly across the left edge of the particle bed located at $x/d_p = 0$. This indicates that apart from the transmitted shock and the reflected wave (shock), there can be other waves inside the particle bed. In this case it appears that there is a stationary wave, since its position in time does not change, located at the leftmost edge of the particle bed. The particle volume fraction changes from 0 to ϕ_1 at the leftmost edge of the particle bed, and this sudden change results in formation of the stationary wave. Mehta *et al.* [19] have studied this stationary wave in detail and described it as the isentropic expansion of the subsonic flow in a converging nozzle. For the simulation parameters considered by Mehta *et al.* [18] in the previous study, they observed that the head of the expansion fan coincides with the stationary wave, resulting in a resonant expansion fan at the leading edge of the particle bed. The combination of these two waves results in a sudden jump in flow properties at the leading edge of the particle curtain.

The x-t plots of the nondimensional streamwise velocity are presented in Fig. 7. The overall qualitative behavior is similar to that of the pressure plots. The signature of the oscillations inside

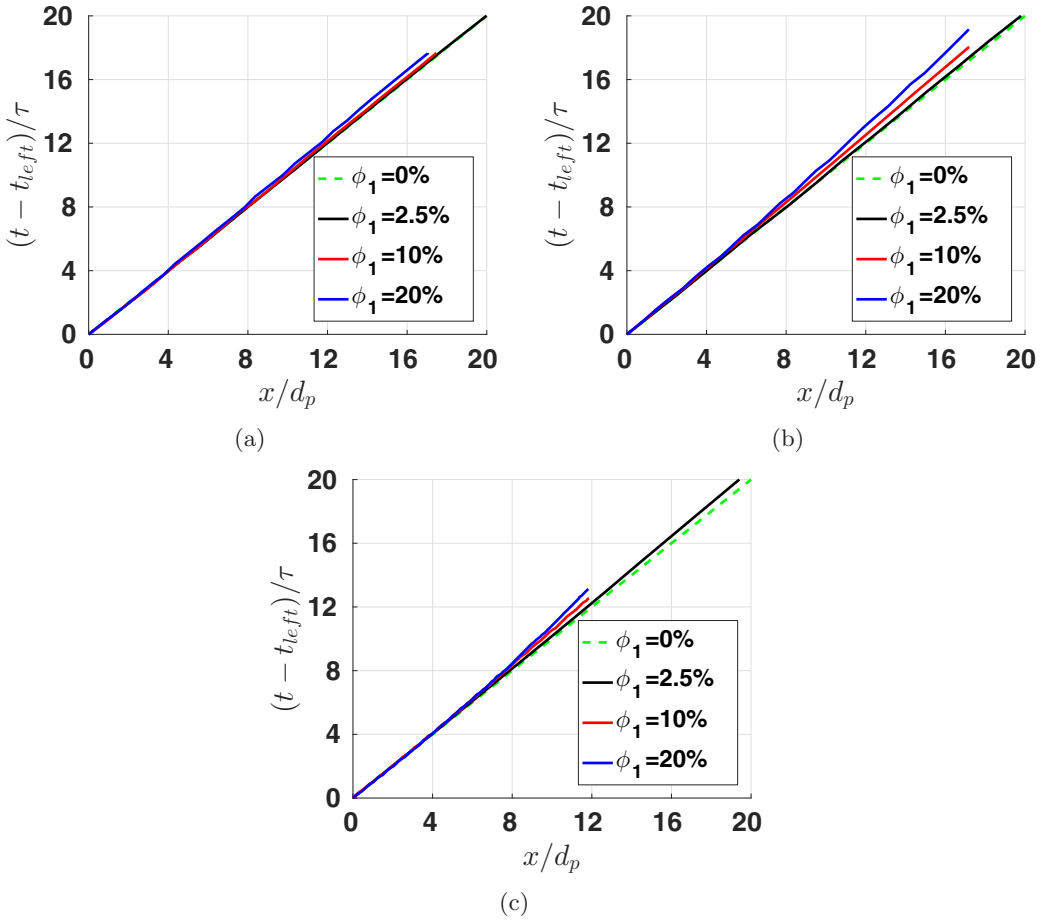

FIG. 8. The x-t plot of the transmitted shock for (a) $M_s = 1.22$, (b) $M_s = 1.66$, and (c) $M_s = 3$.

the particle bed is more pronounced in Fig. 7 compared to Fig. 6. The overall qualitative behavior of the cross-sectional average density x-t plots is similar to that of the pressure and velocity plots and hence not shown here.

C. Slowing down of the transmitted shock

To quantify the effect of the particles on the transmitted shock, we compute its location as a function of time. To determine the location of the transmitted shock we compute the gradient of the cross-sectional averaged pressure. A large spike in the gradient of pressure represents the location of the transmitted shock. The x-t plots for the transmitted shock for $M_s = 1.22$, 1.66, and 3 are plotted in Figs. 8(a), 8(b), and 8(c), respectively. The y axis for these plots has been shifted such that $(t - t_{\text{left}})/\tau = 0$ when the incident shock arrives at the leftmost edge of the particle bed. The dashed green curve in the plots represents the x-t curve for the incident shock in the absence of particles ($\phi_1 = 0\%$) and thus provides a benchmark for comparing the effect of the particles (particle volume fraction) on the speed the transmitted shock.

For the low particle volume fraction case of 2.5% (black curve) and $M_s = 1.22$ and 1.66, the x-t plot coincides with the dashed green curve, indicating that the transmitted shock does not slow down for these cases, but for $M_s = 3$ we can see it slows down slightly at later times. Through this behavior we can clearly observe the effect of postincident-shock Mach number on the decay and

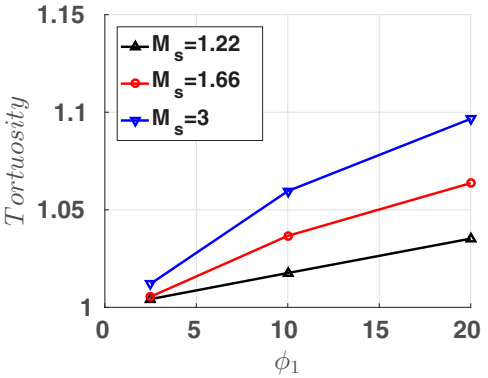

FIG. 9. Plot of tortuosity as a function of particle volume fraction for $M_s = 1.22$ (black curve), $M_s = 1.66$ (red curve), and $M_s = 3$ (blue curve).

eventual slowing down of the transmitted shock even for low particle volume fractions. For $M_s = 1.22$ and $\phi_1 = 10\%$ and 20%, we can observe that the transmitted shock slows down slightly at later times. This behavior is the same for $M_s = 1.66$ and 3 and the effect of particles on slowing down the transmitted shock is even more pronounced due to the formation of bow shocks and shocklets. For $M_s = 1.66$ and 3.0 the slowing down of the transmitted shock is partly due its decay caused by energy dissipation because of formation of shocklets and bow shocks inside the particle bed. However, it is interesting to observe the slowing down of the transmitted shock for $M_s = 1.22$ and $\phi_1 = 10\%$ and 20%. For these two cases, the flow could locally reach supercritical or sonic velocities due to nozzling in the converging channels formed locally by the particles. Locally supercritical flow would result in dissipation of energy because of formation of shocklets, which can contribute to decay and slowing down of the transmitted shock.

At low Mach numbers a more important physical mechanism responsible for slowing down the transmitted shock is tortuosity. Tortuosity is defined as the ratio of the length of the actual flow path of the fluid particles to the shortest path length in the streamwise direction. Tortuosity highlights the local complexity of flow paths through the particle bed. The effect of tortuosity on shock propagation through porous media has been previously investigated by a number of researchers [25,26]. Here we are interested in exploring the effect of tortuosity on slowing down of the transmitted shock. Following Matsumura and Jackson [27], we define tortuosity as

$$T = \frac{\overline{u_{\text{mag}}}}{\overline{|u|}}, \tag{4}$$

where u_{mag} is the magnitude of the velocity ($u_{\text{mag}} = \sqrt{u^2 + v^2 + w^2}$) and the overbar signifies the average taken over the entire particle bed. We compute the tortuosity at the final time when the transmitted shock is close to the farthest end of the particle bed. The part of computational domain that does not include the particle bed has been neglected while computing the tortuosity. A higher value of tortuosity indicates that a parcel of fluid will have to travel more in the transverse direction than it will for a case which has lower tortuosity. Hence, a higher value of tortuosity indicates that the flow in the streamwise direction will be slower and thus it is partly responsible for slowing down of the transmitted shock as measured in terms of its streamwise propagation. We plot tortuosity as a function of particle volume fraction in Fig. 9 for all three incident-shock Mach numbers. For a given incident-shock Mach number the tortuosity increases as the particle volume fraction increases. This is expected since increasing particle volume fraction makes the particle bed more tortuous and hence results in slowing down of the transmitted shock. However, it is interesting to observe that for fixed particle volume fraction, the tortuosity increases as the incident-shock Mach number increases. This can be interpreted as the magnitude of transverse velocities v and w increases at a higher rate as

compared to the increase in the streamwise velocity as the incident-shock Mach number increases. The values of tortuosity presented in Fig. 9 are consistent with the results of slowing down of the transmitted shock presented in Fig. 8.

D. Streamwise drag force

In the previous sections we studied the complex flow field that is set up inside the particle bed due to propagation of an incident shock. In this section we study the effect of the flow field on the particles in terms of the forces experienced by them. There is a rapid increase in the drag force experienced by a single particle when a shock wave starts interacting with it. The streamwise drag force reaches its peak value (first peak) when the incident shock is just about halfway across the particle and then it starts to decrease rapidly as the shock travels completely over the particle. The postincident-shock drag force depends on the postincident-shock flow and its Mach number. The qualitative behavior of the drag force histories for the particles in the random pack are similar to that of an isolated particle and any difference between them is due to the presence of multiple particles in the random pack. The streamwise drag force histories for all the particles in the computational domain are plotted in Figs. 10–12. Since the incident shock travels at a finite speed and the particle bed also has a finite thickness in the streamwise direction, each particle interacts with the incident shock at a different time with respect to the simulation start time. Therefore, the time axis for Fig. 10 is shifted based on the incident or transmitted shock arrival time for each particle such that $(t - t_{\text{arrival}})/\tau = 0$ when the incident shock arrives at the left stagnation point of the particle. Shifting the time axis aligns the initial rise in the streamwise drag force for all the particles. The streamwise drag force after $(t - t_{\text{arrival}})/\tau > 2$ appears to be tangled in appearance due the reflected waves from neighboring particles interacting with each other. The force histories plotted in Fig. 10 are normalized by the corresponding peak force, $C_{D,\text{peak}}$ (first peak), experienced by each particle when the incident or transmitted shock is interacting with the particle.

Results for $M_s = 1.22$ and $\phi_1 = 2.5\%$, 10%, and 20% are plotted in Figs. 10(a)–10(c), respectively. From these plots we can observe that the peak normalized force experienced by most of the particles is 1.0. This is an artifact of the normalization, since the peak force experienced by most of the particles is induced by the incident shock. It is interesting to note that scaling the force histories by their corresponding incident-shock-induced peak force $C_{D,\text{peak}}$ does not make all the force histories collapse on each other at later times. This indicates that there is no perfect correlation between the peak streamwise drag force and the drag force at later times and the "favorable" conditions which result in high peak streamwise force may not hold at later times. This is due to the highly unsteady and transient nature of the flow.

Comparing the results from Figs. 10(a)–10(c) against the drag force experienced by an isolated particle, we can observe the effect of particle volume fraction on the streamwise drag force. For $\phi_1 = 2.5\%$ the magnitude of the streamwise drag force at later times $[(t - t_{\text{arrival}})/\tau > 2]$ is quite small and gradually approaches zero. For higher particle volume fractions, $\phi_1 = 10\%$ and 20%, the magnitude of the postincident-shock drag force is higher compared to the $\phi_1 = 2.5\%$ case. In addition, there is also much higher particle-to-particle variability. This behavior indicates that as the particle volume fraction increases, the strength of the secondary wave interactions and wakes inside the particle bed also increases as observed in Figs. 6 and 7. The reflected waves have to travel farther in space in order to reach the neighboring particles for the low particle volume fraction case compared to the higher particle volume fraction cases. Hence, for the low particle volume case, the impact of the reflected waves on the streamwise drag force at later times is small since oscillations decay. It is also clear that the strength of the reflected waves decreases at later times, indicating that an equilibrium state can be achieved eventually. When the equilibrium state is achieved, the oscillations inside the particle bed will decay and the postincident-shock drag force will be zero for all the particles. The possibility and the time it will take to reach the equilibrium state will depend on the particle volume fraction and the postincident-shock Mach number.

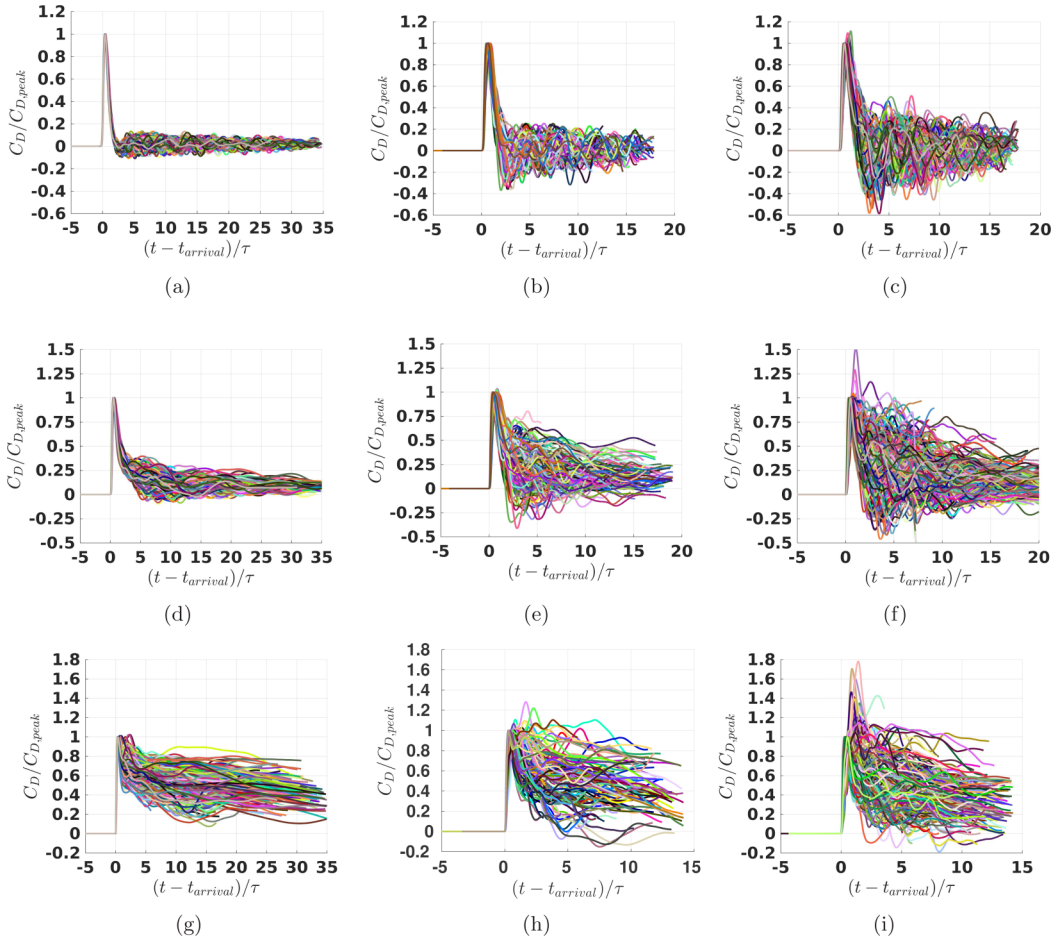

FIG. 10. Plot of the normalized nondimensional drag force C_D as a function of nondimensional shifted time $(t - t_{\text{arrival}})/\tau$ for $\phi_1 = 2.5\%$, 10%, and 20% and (a)–(c) $M_s = 1.22$, (d)–(f) $M_s = 1.66$, and (g)–(i) $M_s = 3$, respectively.

The force histories for all the particles for an incident-shock Mach number of $M_s = 1.66$ and 3 are presented in Figs. 10(d)–10(f) and 10(g)–10(i), respectively. The overall behavior of the force histories is similar to that discussed previously for $M_s = 1.22$. For an incident shock of $M_s = 1.66$ and 3 the postincident-shock Mach number is supercritical. Owing to this, the postincident-shock flow accelerates to locally sonic or supersonic velocities around the particles and result in the formation of shocklets and bow shocks as seen in Figs. 4 and 5. The formation of shocklets and or bow shocks around the particles results in nonzero streamwise drag force on the particles at later times.

In Fig. 10 we can observe that some of the particles have peak streamwise drag force substantially higher than $C_{D,\text{peak}}$. In Fig. 11 we plot the force histories of some of the particles which have normalized streamwise drag force $C_D/C_{D,\text{peak}}$ greater than 1.0 for the $\phi_1 = 20\%$ and $M_s = 3$ case. The shifted time axis has been plotted on a logarithmic scale. From this figure we can observe that the normalized streamwise drag force increases from zero to 1.0 initially when the incident or transmitted shock is just about halfway across the particle. This is the first peak that a particle experiences and it is induced by the incident or transmitted shock. At later times the normalized streamwise drag force increases beyond 1.0 for some of the particles. This increase in drag force is

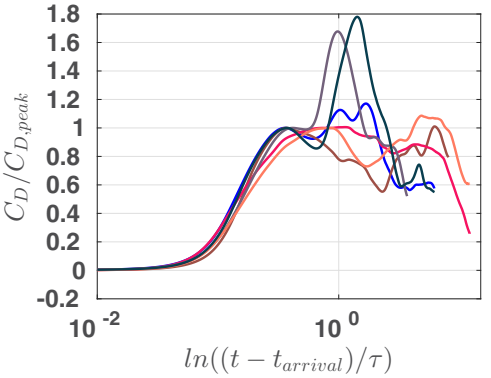

FIG. 11. Plot of the normalized drag coefficient $C_D/C_{D,\text{peak}}$ as a function of logarithmic shifted nondimensional time $\log[(t - t_{\text{arrival}})/\tau]$ for six particles in the random bed for $M_s = 3$ and $\phi_1 = 20\%$.

due to the fluid-mediated particle-particle interactions (secondary wave interactions). Some of the particles have drag forces up to 80% higher than $C_{D,\text{peak}}$. As mentioned previously, point-particle force models are used for simulating flows with millions of particles. These point-particle models are derived or generated for a single particle; i.e., they predict the drag force on each particle in the particle bed as if every particle is isolated. This induces an inherent error by not accounting for the variation in the drag force due to the presence of neighboring particles. It is clear from the normalized force history plots that the secondary wave interactions and fluid-mediated particle-particle interactions can result in significantly higher forces than $C_{D,\text{peak}}$. These higher forces can significantly alter the particle motion and the overall flow and need to be accounted for when developing point-particle force models.

In Figs. 10 and 11 we can clearly observe the particle-to-particle variability in the postincident-shock drag force, but it is difficult to observe the variation in the peak drag force because of the normalization and shifting of the time axis. To characterize the effect of the incident shock on the particles and to condense the information from the force history plots, we plot only the $C_{D,\text{peak}}$ (first peak) for each particle for all particle volume fractions and $M_s = 1.22$, 1.66, and 3 in Figs. 12(a), 12(b), and 12(c), respectively. The x axis for these plots is the nondimensional streamwise location of the corresponding particle. It can be observed from these figures that there is a substantial particle-to-particle variation in $C_{D,\text{peak}}$. The reason for this particle-to-particle variation is the random distribution of particles; every particle has a unique neighborhood of particles surrounding it, which modifies the incident shock and results in a slightly different $C_{D,\text{peak}}$ for that particle. The mean strength of the transmitted shock varies as it travels through the particle bed and that also causes fluctuations in the values of $C_{D,\text{peak}}$.

To gain insight into the varying strength of the transmitted shock we obtain an exponential fit for the $C_{D,\text{peak}}$ data. It is plotted as the solid line in Fig. 12. The exponential fit is given by

$$\langle C_{D,\text{peak}} \rangle = a \exp^{-b(x/d_p)} + c, \tag{5}$$

where a, b, and c are the fit parameters. The exponential fit can be thought of as the mean peak drag force at a particular streamwise location in the particle bed and hence it can also be interpreted as the mean shock strength at that streamwise location.

For $M_s = 1.66$ and 3.0 and all the particle volume fraction cases, the mean $C_{D,\text{peak}}$ decreases as a function of the streamwise location. This behavior is expected since the postincident-shock Mach numbers are supercritical for these incident-shock Mach numbers and that causes dissipation of energy because of formation of bow shocks and shocklets. For a fixed incident-shock Mach number the rate of decrease of mean $C_{D,\text{peak}}$ increases as the particle volume fraction increases. For

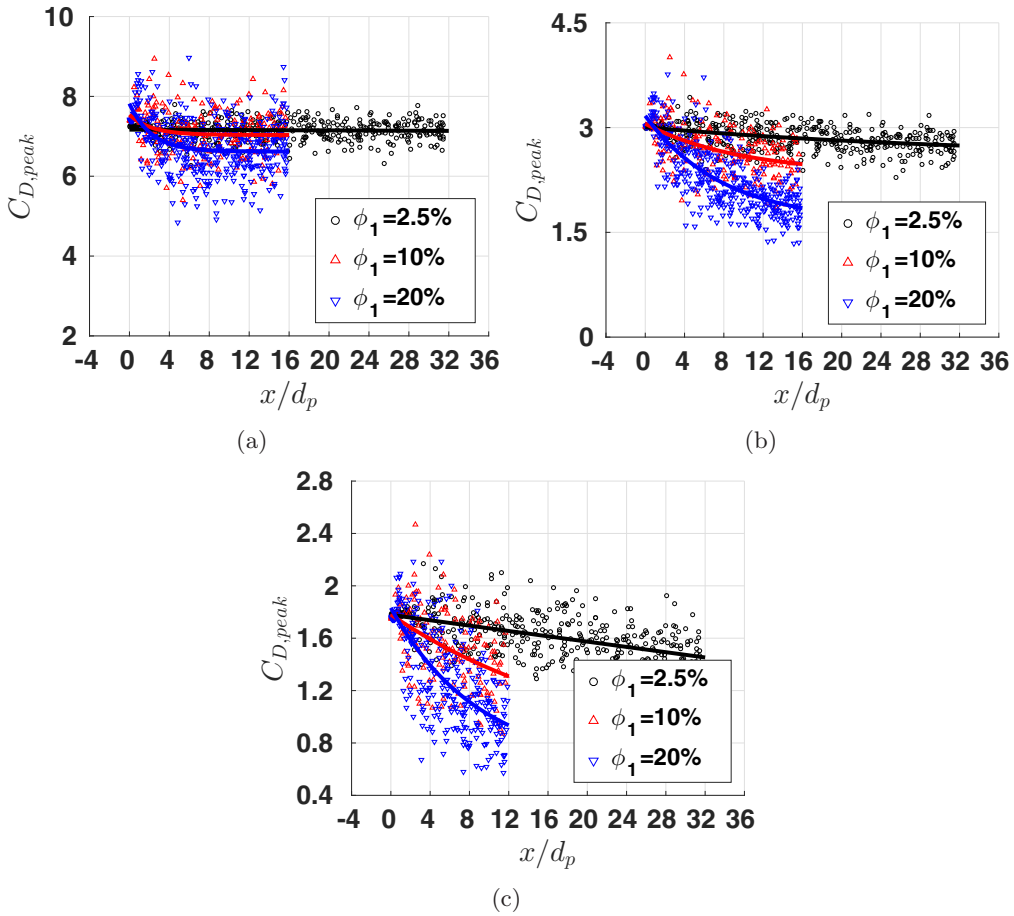

FIG. 12. Plot of the peak drag coefficient $C_{D,\text{peak}}$ along with the exponential curve fit for $\phi_1 = 2.5\%$, $\phi_1 = 10\%$, $\phi_1 = 20\%$, and (a) $M_s = 1.22$, (b) $M_s = 1.66$, and (c) $M_s = 3$.

$M_s = 1.22$ and $\phi_1 = 2.5\%$ the mean $C_{D,\text{peak}}$ is nearly constant, indicating that the mean strength of the transmitted shock remains constant as it travels through the particle bed. However, it is interesting to observe that for $M_s = 1.22$ and $\phi_1 = 10\%$ and 20% there is a sharp decrease in the mean $C_{D,\text{peak}}$ initially (close to the front edge of the particle bed) and then it reaches a near constant value. The particles close to the front edge of the particle bed interact with an undisturbed planar shock and the $C_{D,\text{peak}}$ for these particles is close to that of an isolated particle. Once the shock travels over these first plane of particles it deforms as it wraps around the particles. This is the "entry" effect. For high particle volume fractions (10% and 20%) the transmitted shock is always slightly deformed as it is traveling through the particle bed. For the case of $M_s = 1.22$ the amount of dissipation is quite small resulting in a "steady" state for the transmitted shock and hence the slope the mean $C_{D,\text{peak}}$ is nearly constant after a few diameters inside the particle bed. For higher incident-shock Mach numbers (1.66 and 3) its hard to observe the entry effect due to the bulk effect of the particles on the transmitted shock. For these incident-shock Mach numbers there is dissipation resulting in weakening of the transmitted shock and hence negative slope for $\langle C_{D,\text{peak}} \rangle$.

In Figs. 12(b) and 12(c) we observe a large variation in the peak drag force experienced by each particle. The physical mechanisms for particles experiencing variable drag force have been previously discussed by Mehta *et al.* [18,19]. They attributed the local variations in the peak drag force to be due to either a constructive or a destructive interference of the shock wave. In other

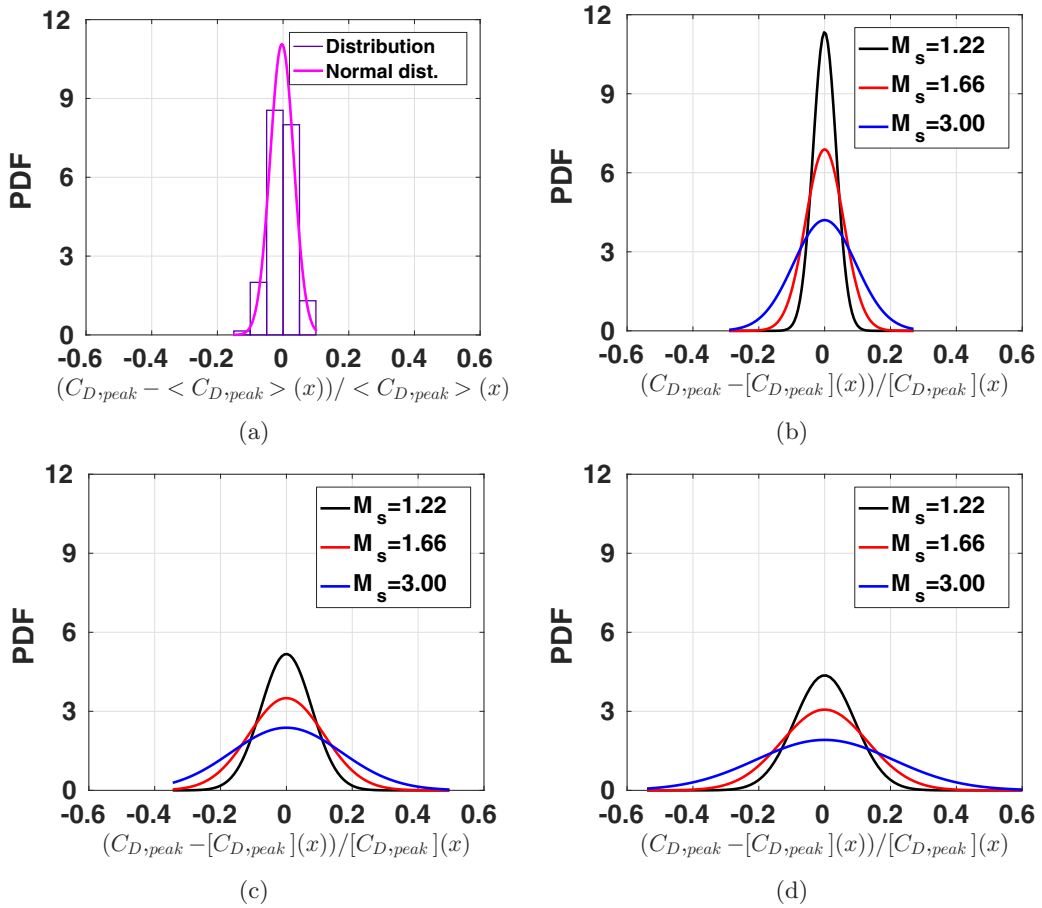

FIG. 13. Plot of the normal distribution fit for the fluctuating peak drag coefficient for (a) $M_s = 1.22$ and $\phi_1 = 2.5\%$, (b) $\phi = 2.5\%$, (c) $\phi = 10\%$, and (d) $\phi = 20\%$.

words, shock focusing leads to an increase in the peak drag force and shock defocusing results in a decrease. Following Mehta *et al.* [19], we compute the local fluctuation in $C_{D,\text{peak}}$. It is given by

$$C_{D,flu_i} = [C_{D,\text{peak}} - [C_{D,\text{peak}}](x)]/[C_{D,\text{peak}}](x), \tag{6}$$

where $[C_{D,\text{peak}}](x)$ is obtained from the linear (least-squares) fit for the $C_{D,\text{peak}}$ data. The histogram of the fluctuating peak drag force for $\phi_1 = 2.5\%$ and $M_s = 1.22$ is plotted in Fig. 13(a). The mean and standard deviation for the distribution is computed and a normal distribution fit for the fluctuating $C_{D,\text{peak}}$ data is obtained. The magenta curve in Fig. 13(a) is the normal fit for the data. The normal fits for $M_s = 1.22$ (black curve), $M_s = 1.66$ (red curve), and $M_s = 3$ (blue curve) are plotted for $\phi_1 = 2.5\%$, 10%, and 20% in Figs. 13(b), 13(c), and 13(d), respectively. Through these plots we can observe the impact of the particle volume fraction and the incident-shock Mach number on the fluctuations in $C_{D,\text{peak}}$. We can observe that for all the cases considered here, the fluctuations in the peak drag force follow a Gaussian like distribution. The x axis in the plot can be thought of as the percentage variation in $C_{D,\text{peak}}$. The percentage variation in $C_{D,\text{peak}}$ increases as the incident-shock Mach number and the particle volume fraction increase. The fact that the variation in the peak drag force follows a Gaussian-like distribution can be helpful in improving the current point-particle drag models. For example, we can add a stochastic variation (bound by the Gaussian

distribution) to the mean peak drag force predicted by the existing model to capture the variation in the peak drag force.

E. Lift forces

As the incident or transmitted shock travels through the particle bed, it deforms when it wraps around the particles as seen in Figs. 4 and 5. This local deformation is on the particle length scale (particle diameter) and disrupts the planarity of the shock wave. Nonplanar oblique shocks induce transverse or lift forces on the particles. Another important physical mechanism responsible for transverse forces experienced by the particles is the unsteady flow inside the particle bed as a result of the random distribution of the particles. It has been previously discussed by Mehta *et al.* [18] that lift forces for a transverse periodic face-centered-cubic array of particles are zero. Thus, it should be noted that in the case of an incident shock interacting with certain arrangement of particles, lift forces can be zero (it depends on the arrangement of the particles). In the present study we have a random distribution of particles, which results in random fluctuations in the flow field and hence transverse forces on the particles. The lift force in the y direction, $C_{D,y}$, experienced by all the particles in the domain for $M_s = 1.22$ is plotted in Figs. 14(a)–14(c), for $M_s = 1.66$ in Figs. 14(d)–14(f), and for $M_s = 3$ in Figs. 14(g)–14(i), for $\phi_1 = 2.5\%$, 10%, and 20%, respectively. The lift force in the z direction has similar overall behavior and magnitude compared to $C_{D,y}$ and hence is not shown here. The lift forces exhibit tangled behavior, similar to that shown by the streamwise drag force C_D. For most of the particles the lift forces are nonzero at $(t - t_{\text{arrival}})/\tau = 0$. This indicates that the transmitted shock induces some lift force on the particles when it interacts with them. This is possible only if the transmitted shock is locally oblique when it interacts with the particles. However, it is interesting to note that the peak lift force for particles do not align with each other after shifting the time axis as they did for the streamwise drag force in Fig. 10. This behavior indicates that the fluctuations in the flow, at later times, generated by the random distribution of the particles can lead to substantial lift forces. Thus, the magnitude and instance when the peak lift force occurs depend on the local neighborhood of the particles and vary from particle to particle. For a fixed incident-shock Mach number, the magnitude of the lift force increases as the particle volume fraction increases. For all the cases considered in this study, we can see that the mean lift force as a function of time will be close to zero. However, it is important to note that the lift forces can be 20%–40% of the streamwise drag force and hence will play a big role in the motion of the particles and shock transmission. Traditionally, numerical simulations of incident shock interacting with particles that employ point-particle force models do not account for the lift forces on the particles.

IV. CONCLUSION

In this paper we studied the effect of an incident shock interacting with multiple particles. Fully resolved three-dimensional inviscid simulations of shock traveling through a bed of particles were carried out. A uniform random distribution of particles was considered and both the incident-shock Mach number and the particle volume fraction were varied. We plotted the contour plots of pressure, Mach number, and vorticity magnitude to identify the complex physical mechanism at play during shock-particle interaction. The baroclinic mechanism of vorticity generation was responsible for the vorticity inside the particle bed and it was generated due to breakage of symmetry by the random distribution of the particles. We computed the cross-sectional average of flow quantities to identify the complex wave structure inside the particle bed to characterize the strength the reflected waves and transmitted shock. The transmitted shock weakened as it traveled through the particle bed for all the cases with supercritical postincident-shock flow. In terms of decrease in the mean peak drag force (as a function of streamwise location) and overall weakening of the transmitted shock, there is not much difference between supersonic and supercritical postincident-shock flow cases. The postincident-shock flow being supercritical had a major impact on the transmitted shock weakening and that also resulted in a decrease in the mean peak drag force.

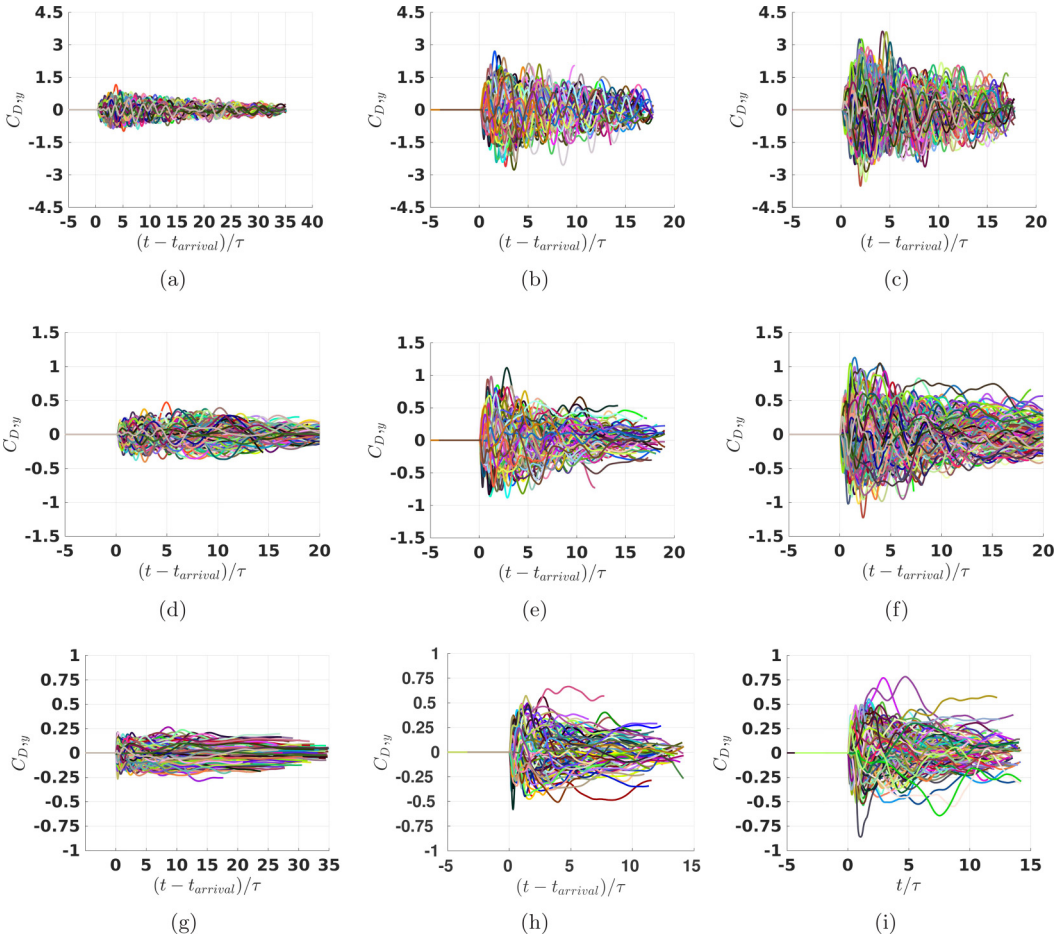

FIG. 14. Plot of the nondimensional y lift force $C_{D,y}$ as a function of the nondimensional shifted time $(t - t_{\text{arrival}})/\tau$ for $\phi_1 = 2.5\%$, 10%, and 20% and (a)–(c) $M_s = 1.22$, (d)–(f) $M_s = 1.66$, and (g)–(i) $M_s = 3$, respectively.

The presence of multiple particles altered the force history of each particle compared to the force history of a single isolated particle for a given incident shock. We plotted the peak streamwise drag force $C_{D,\text{peak}}$ for each particle to characterize the variability in the drag force and computed the mean peak drag force as a function the streamwise location. The streamwise drag force histories of all the particles were normalized by the peak drag force each particle experienced due to the incident or transmitted shock. We observed that this normalization did not result in collapse of the force histories on top of each other, indicating that there is no perfect correlation between the peak drag force and the drag force at later times. We also observed that some of the particles had normalized peak drag forces greater than 1. This behavior was a result of fluid-mediated particle-particle interaction, which can lead to forces higher than $C_{D,\text{peak}}$ after the incident or transmitted shock has traveled around the particle.

Based on our findings, we postulate that significant improvements can be made to current point-particle force models used in Euler-Lagrange simulations. The current point-particle force models cannot capture the variability in the drag force and cannot predict forces greater than $C_{D,\text{peak}}$, because they are derived for a single isolated particle. We can make simple improvements to the point-particle models such as adding a stochastic force (bound by the Gaussian fit) to the varying

mean peak drag force to capture the variability in the peak drag force. Other improvements would be to include lift forces and account for rotational forces on the particles due to the vorticity inside the particle bed.

ACKNOWLEDGMENTS

This work was performed under the auspices of the U.S. Department of Energy by Lawrence Livermore National Laboratory under Contract No. DE-AC52-07NA27344, IM review LLNL-JRNL-751463. This work was also supported in part by the U.S. Department of Energy, National Nuclear Security Administration, Advanced Simulation and Computing Program, as a Cooperative Agreement under the Predictive Science Academic Alliance Program, under Contract No. DE-NA0002378. S.B. was also supported in part by the Defense Threat Reduction Agency, Basic Research Award No. HDTRA1-14-1-0028 to University of Florida.

[1] C.-D. Ohl, M. Arora, R. Ikink, M. Delius, B. Wolfrum, and T. P. Insitute, *Proceedings of the Fifth International Symposium on Cavitation*, Osaka, 2003 (unpublished), p. 1.

[2] E. Del Prete, A. Chinnayya, L. Domergue, A. Hadjadj, and J.-F. Haas, Blast wave mitigation by dry aqueous foams, Shock Waves **23**, 39 (2013).

[3] M. Grujicic, W. C. Bell, B. Pandurangan, and P. S. Glomski, Fluid/structure interaction computational investigation of blast-wave mitigation efficacy of the advanced combat helmet, J. Mater. Eng. Perform. **20**, 877 (2011).

[4] Z. Su, W. Peng, Z. Zhang, G. Gogos, R. Skaggs, and B. Cheeseman, Numerical simulation of a novel blast wave mitigation device, Int. J. Impact Eng. **35**, 336 (2008).

[5] J. Richmond, I. Liebman, A. Bruszak, and L. Miller, A physical description of coal mine explosions. Part II, Symp. (Int.) Combust. **17**, 1257 (1979).

[6] S. Carcano, L. Bonaventura, T. Esposti Ongaro, and A. Neri, A semi-implicit, second-order-accurate numerical model for multiphase underexpanded volcanic jets, Geosci. Model Dev. **6**, 1905 (2013).

[7] I. Tsuyoshi, Y. Ryo, and I. Shu-Ichiro, Turbulence and magnetic field amplification in supernova remnants: Interactions between a strong shock wave and multiphase interstellar medium, Astrophys. J. **695**, 825 (2009).

[8] O. Igra and K. Takayama, Shock tube study of the drag coefficient of a sphere in a non-stationary flow, Proc. R. Soc. London Ser. A **442**, 231 (1993).

[9] A. Britan, T. Elperin, O. Igra, and J. P. Jiang, Acceleration of a sphere behind planar shock waves, Exp. Fluids **20**, 84 (1995).

[10] H. Tanno, K. Itoh, T. Saito, A. Abe, and K. Takayama, Interaction of a shock with a sphere suspended in a vertical shock tube, Shock Waves **13**, 191 (2003).

[11] H. Tanno, T. Komuro, M. Takahashi, K. Takayama, H. Ojima, and S. Onaya, Unsteady force measurement technique in shock tubes, Rev. Sci. Instrum. **75**, 532 (2004).

[12] M. Sun, T. Saito, K. Takayama, and H. Tanno, Unsteady drag on a sphere by shock wave loading, Shock Waves **14**, 3 (2005).

[13] H. Naiman and D. D. Knight, The effect of porosity on shock interaction with a rigid, porous barrier, Shock Waves **16**, 321 (2007).

[14] J. Regele, J. Rabinovitch, T. Colonius, and G. Blanquart, Unsteady effects in dense, high speed, particle laden flows, Int. J. Multiphase Flow **61**, 1 (2014).

[15] Z. Hosseinzadeh-Nik, S. Subramaniam, and J. D. Regele, Investigation and quantification of flow unsteadiness in shock-particle cloud interaction, Int. J. Multiphase Flow **101**, 186 (2018).

[16] P. Sridharan, T. L. Jackson, J. Zhang, and S. Balachandar, Shock interaction with one-dimensional array of particles in air, J. Appl. Phys. **117**, 075902 (2015).

[17] Y. Mehta, T. L. Jackson, J. Zhang, and S. Balachandar, Numerical investigation of shock interaction with one-dimensional transverse array of particles in air, J. Appl. Phys. **119**, 104901 (2016).
[18] Y. Mehta, C. Neal, T. L. Jackson, S. Balachandar, and S. Thakur, Shock interaction with three-dimensional face centered cubic array of particles, Phys. Rev. Fluids **1**, 054202 (2016).
[19] Y. Mehta, C. Neal, K. Salari, T. L. Jackson, S. Balachandar, and S. Thakur, Propagation of a strong shock over a random bed of spherical particles, J. Fluid Mech. **839**, 157 (2018).
[20] M. Parmar, A. Haselbacher, and S. Balachandar, Modeling of the unsteady force for shock-particle interaction, Shock Waves **19**, 317 (2009).
[21] M. Parmar, A. Haselbacher, and S. Balachandar, Generalized Basset-Boussinesq-Oseen Equation for Unsteady Forces on a Sphere in a Compressible Flow, Phys. Rev. Lett. **106**, 084501 (2011).
[22] M. Parmar, A. Haselbacher, and S. Balachandar, Equation of motion for a sphere in non-uniform compressible flows, J. Fluid Mech. **699**, 352 (2012).
[23] S. Annamalai and S. Balachandar, Faxen form of time-domain force on a sphere in unsteady spatially varying viscous compressible flows, J. Fluid Mech. **816**, 381 (2017).
[24] C. H. Rycroft, VORO++ : A three-dimensional Voronoi cell library in C++, Chaos **19**, 041111 (2009).
[25] H. Li, A. Levy, and G. Ben-Dor, Head-on interaction of planar shock waves with ideal rigid open-cell porous materials. analytical model, Fluid Dyn. Res. **16**, 203 (1995).
[26] M. W. Seitz and B. W. Skews, Effect of compressible foam properties on pressure amplification during shock wave impact, Shock Waves **15**, 177 (2006).
[27] Y. Matsumura and T. L. Jackson, Numerical simulation of fluid flow through random packs of cylinders using immersed boundary method, Phys. Fluids **26**, 043602 (2014).